This article was downloaded by: *[Oak Ridge National Laboratory]*
On: *15 August 2008*
Access details: *Access Details: [subscription number 759359076]*
Publisher *Taylor & Francis*
Informa Ltd Registered in England and Wales Registered Number: 1072954 Registered office: Mortimer House, 37-41 Mortimer Street, London W1T 3JH, UK

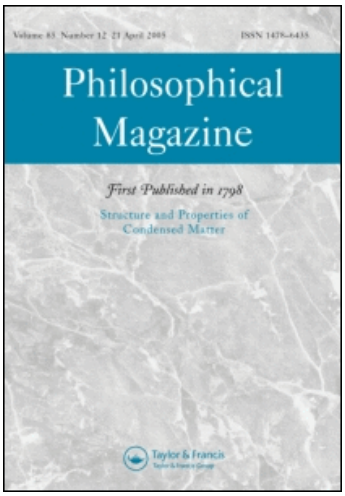

Philosophical Magazine
Publication details, including instructions for authors and subscription information:
http://www.informaworld.com/smpp/title~content=t713695589

Direct imaging of dislocation core structures by Z-contrast STEM

M. F. Chisholm [a]; S. J. Pennycook [a]
[a] Condensed Matter Sciences Division, Oak Ridge National Laboratory, Oak Ridge, TN 37831-6031, USA

Online Publication Date: 11 October 2006

To cite this Article Chisholm, M. F. and Pennycook, S. J.(2006)'Direct imaging of dislocation core structures by Z-contrast STEM',Philosophical Magazine,86:29,4699 — 4725

To link to this Article: DOI: 10.1080/14786430600778757

URL: http://dx.doi.org/10.1080/14786430600778757

PLEASE SCROLL DOWN FOR ARTICLE

Full terms and conditions of use: http://www.informaworld.com/terms-and-conditions-of-access.pdf

This article may be used for research, teaching and private study purposes. Any substantial or systematic reproduction, re-distribution, re-selling, loan or sub-licensing, systematic supply or distribution in any form to anyone is expressly forbidden.

The publisher does not give any warranty express or implied or make any representation that the contents will be complete or accurate or up to date. The accuracy of any instructions, formulae and drug doses should be independently verified with primary sources. The publisher shall not be liable for any loss, actions, claims, proceedings, demand or costs or damages whatsoever or howsoever caused arising directly or indirectly in connection with or arising out of the use of this material.

Philosophical Magazine,
Vol. 86, Nos. 29–31, 11 Oct.–1 Nov. 2006, 4699–4725

Taylor & Francis
Taylor & Francis Group

Direct imaging of dislocation core structures by Z-contrast STEM

M. F. CHISHOLM and S. J. PENNYCOOK*

Condensed Matter Sciences Division, Oak Ridge National Laboratory,
Oak Ridge, TN 37831-6031, USA

(*Received 17 March 2006; in final form 20 April 2006*)

The development of Z-contrast imaging in the scanning transmission electron microscope has enabled dislocation core structures to be visualized with increasing detail. In single-component systems, core structures have been generally found to be as expected from simple considerations or theoretical predictions. In more complex structures, however, cores are generally seen to take on configurations that were not previously anticipated, utilizing reconstructions or non-stoichiometry to lower the elastic strain field. We present an overview of these developments in a variety of materials. In suitable circumstances, impurity segregation sites have been directly imaged at dislocation cores. More generally, electron energy loss spectroscopy gives detailed, atomic-resolution information on stoichiometry and impurity concentrations. These additional variables introduce additional degrees of freedom into the whole issue of structure/property relationships. We show examples of an impurity-induced core structure transformation and a cooperative doping effect. First-principles density functional calculations are used to link observed core structures to macroscopic properties. We also show that planar dislocation arrays are accurate descriptions of tilt grain boundaries, with the structural units geometrically equivalent to individual dislocation cores.

Downloaded By: [Oak Ridge National Laboratory] At: 16:07 15 August 2008

1. Introduction

One of the great successes of transmission electron microscopy was (and continues to be) the observation of dislocations. Dislocations were first introduced as postulated local modifications of a material which are transferred through that material as a response to strain, e.g. [1]. In the development of the theory of deformation of materials, dislocations were initially a geometric construct, a localized boundary of misfit between adjoining packets of material. This treatment was further developed as a means to accommodate misfit, firstly, between two misoriented crystals of the same material [2, 3], and secondly, at the interface between dissimilar materials, e.g. epitaxial thin films [4]. In 1956, Bollmann [5] and Hirsch *et al.* [6] independently discovered that dislocations could be observed by transmission electron microscopy. The dislocations were seen by means of diffraction contrast arising from the strain field of the dislocations. The more direct method

*Corresponding author. Email: pennycooksj@ornl.gov

Philosophical Magazine
ISSN 1478–6435 print/ISSN 1478–6443 online © 2006 Taylor & Francis
http://www.tandf.co.uk/journals
DOI: 10.1080/14786430600778757

of observing dislocations is to use an electron microscope with higher resolution than the spacing of the crystal planes being imaged. Interestingly, this was also first achieved (earlier) in 1956 by Menter [7] on thin crystals of copper and platinum phthalocyanine with planar spacings of ~1.2 nm.

Although a dislocation may be characterized by its Burgers vector, line direction and slip plane, there are a large number of possible dislocation core structures and associated impurity and point defect segregation effects that must be determined to understand the overall role of these defects in determining a material's properties. Fortunately, there are tools for this difficult situation that can provide a true atomic-level understanding of the origin of those properties. One is the technique of Z-contrast imaging in the scanning transmission electron microscope (STEM), which provides a direct image of atomic arrangements (reviews of the technique are given in [8, 9]). Even in the highly strained regions of dislocation cores, atomic structures can be directly determined from experimental data. In the STEM, imaging is achieved using a highly coherent electron beam, which is scanned across the specimen. The transmitted intensity reaching any of a number of possible detectors can be used to form an image. The detector plane contains a coherent diffraction pattern with detailed structure. However, the total scattered intensity is conserved. An image based on total scattered intensity is by definition an incoherent image, free from phase contrast interference effects such as contrast reversals with defocus. Thus, the essential requirement for incoherent imaging is that the detector integrates enough of the diffraction pattern to accurately reflect the total scattered intensity. These conditions are met if the inner angle of the annular detector and the outer angle of the spectrometer aperture are sufficiently large to average a large number of diffracted beams around their perimeters [10, 11]. Both a high-angle annular dark-field detector and a large spectrometer entrance aperture will give incoherent images with a simple and direct correlation with each other and with the specimen. The signal scattered to high angles recorded on an annular dark field (ADF) detector is known as a Z-contrast image because it depends approximately on the mean-square atomic number (Z) in the volume being examined.

The second tool is the ability to stop the STEM probe on an individual atomic column selected from the image and perform electron energy loss spectroscopy (EELS) [12, 13]; one can then extract the local impurity concentration and electronic structure from the core loss fine structure. The combination of atomic-resolution Z-contrast STEM and simultaneous EELS represents a powerful method to link microscopic atomic and electronic structure to macroscopic properties, allowing materials, nanoscale systems and interfaces to be probed with unprecedented detail.

The third invaluable tool is the use of first-principles total-energy calculations. The rapidly increasing computational power makes it possible to perform structural relaxations of configurations suggested from experiment, to determine the local electronic structure and optical properties, and to obtain segregation energies for impurities and point defects. When these tools are applied together an increasingly complete picture of dislocations at the atomic level is generated.

Here, we present an overview of these techniques applied to metals, semiconductors and ceramics. Many of the results are from dislocations in planar arrays, i.e. grain boundaries and heteroepitaxial interfaces. This simplifies the investigations because the dislocations are arranged in periodic or quasiperiodic

Downloaded By: [Oak Ridge National Laboratory] At: 16:07 15 August 2008

arrays, in specific locations and can easily be oriented to image the core structure. Also, arranging the dislocations into a periodic or quasiperiodic array reduces the long-range strain field and associated surface relaxation effects, although such effects are much less severe for Z-contrast imaging than for phase contrast imaging [14], and they can even be useful for locating screw dislocation cores [15]. While models of low-angle grain boundaries and low-misfit interfaces as arrays of dislocations are physically accurate, the validity of these models at large misfits has been questioned. The concern has been that the regions of high misfit of individual dislocations, i.e. their cores rapidly overlap, so that it is impossible to distinguish any individual dislocation core. The use of these new tools has established definitively that, at least for the special classes of boundaries studied, the dislocation cores do indeed remain distinct; they have the same atomic configuration as they would have if isolated in the bulk crystal. The individual dislocation cores can be identified directly from the image, and their projected Burgers' vectors determined by inspection. The dislocation model of grain boundaries [16] is seen to be not just a geometric construction but an accurate atomic-level description of grain boundary structure, as predicted by the structural unit model [17]. The structural units are identifiable dislocation cores. In one example, it is shown that the boundary dislocation cores do not loose their identifiable atomic configurations even when spaced every 0.23 nm along the boundary.

Downloaded By: [Oak Ridge National Laboratory] At: 16:07 15 August 2008

2. Perovskites and related materials

The delivery of the 100-kV VG Microscopes' HB501UX at Oak Ridge National Laboratory coincided nearly exactly with the discovery of high-temperature superconductivity in $YBa_2Cu_3O_{7-x}$ (YBCO). It is, thus, not surprising that many of the initial images obtained on this instrument were from YBCO. As suggested in the original work by Bednorz and Muller [18], and more concretely by Ekin *et al.* [19], the low critical current density and the Josephson behaviour of polycrystalline samples was attributed to grain boundaries. This led to a large number of efforts to first clarify the influence of grain boundaries on the superconducting transport [20–24] and to characterize their structures. It was found that $\langle 100 \rangle$ tilt boundaries consist of an asymmetric array of dislocations each with a total Burgers vector of 1.17 nm, the c lattice parameter of this compound. At low misorientations, these dislocations dissociate into $c/3$ partials, corresponding to the repeat vector of the oxygen sublattice [25]. In the case of a 7.5° boundary, the dislocation cores begin to overlap and appear amorphous, as also seen in the 13.5° boundary shown in figure 1a [26]. It was argued that the structural relaxation of the cores is driven by the large core energy density of the grain boundary dislocations. The triangular core regions appear dark because the structure is non-crystalline. To determine if they have the same average composition as the grain interior, the boundary region was tilted to an off-axis orientation. Uniform contrast was seen along the boundary and into the adjacent grain. This indicates that these amorphous boundary defects are chemically identical to the grain interior and not pockets of segregated impurities [26].

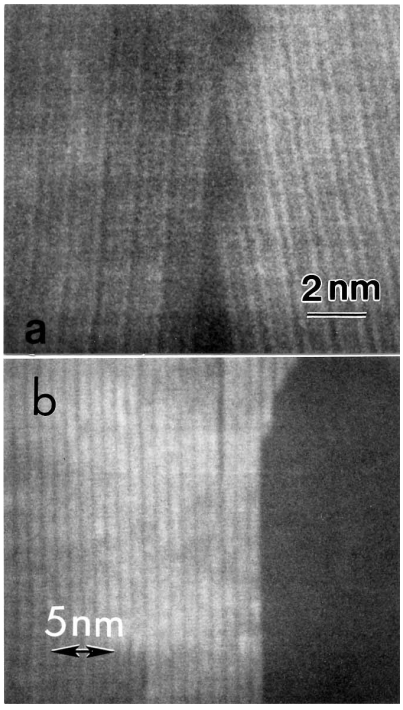

Figure 1. Z-contrast image of a 13° ⟨100⟩ tilt boundary in $YBa_2Cu_3O_{7-x}$. (a) Adjacent grains oriented for electron channelling along the (001) planes, showing an array of triangular amorphous defects at the boundary. (b) Same two grains tilted so that the right-hand grain is not channelling, showing no detectable contrast variations along the grain boundary. This rules out the presence of any of the likely second phases in the triangular defects (image recorded with the 100 kV STEM with 0.22 nm resolution).

Downloaded By: [Oak Ridge National Laboratory] At: 16:07 15 August 2008

The same tendency to form only complete unit blocks of YBCO is also seen in the ⟨001⟩ tilt boundaries. In this case, low angle boundaries were seen to consist of arrays of isolated dislocations ($\boldsymbol{b} = 0.39$ nm) to accommodate the misorientation of the adjacent grains. Figure 2 shows a Z-contrast image of a low angle ⟨001⟩ tilt grain boundary, which is seen to consist of an array of $\boldsymbol{a}\langle 100\rangle$ dislocations. The core structures of the dislocations are directly seen in the image; four take the form of a pentagon of Y/Ba columns with two Cu columns in the center, while one comprises a pentagon of Cu columns with two Y/Ba columns in the core [27]. The O columns are not visible at this resolution.

The electrical activity of grain boundaries is responsible for numerous effects in perovskite-based oxide systems, not only the poor critical currents across grain boundaries in the oxide superconductors, but also the nonlinear *I–V* characteristics useful for capacitors and varistors, the low field colossal magneto-resistance in the lanthanum manganites, and doubtless many other properties, both desired and undesired, in materials with related structures. $SrTiO_3$ represents a model system for understanding the atomic origin of these grain boundary phenomena. In 1994, the atomic structure of a 25° ⟨001⟩ $SrTiO_3$ tilt boundary was determined using

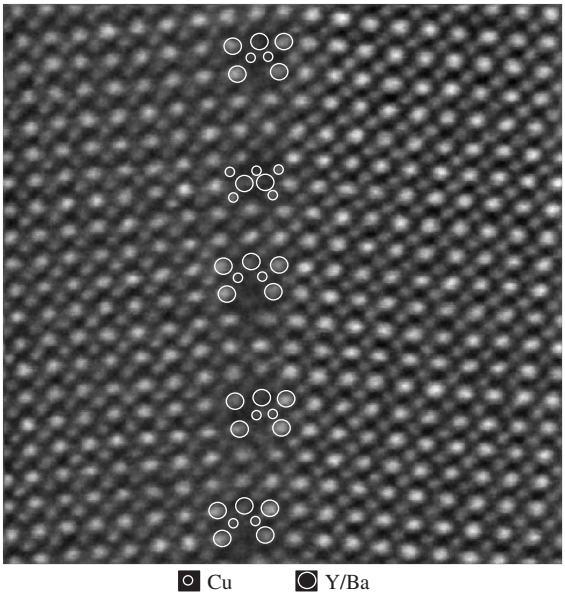

Figure 2. Plan view *Z*-contrast image of a biaxially textured film of YBCO grown on Ni by laser ablation. Bright spots are Y/Ba columns, less bright are Cu columns. This 12° ⟨001⟩ tilt grain boundary comprises an almost regular array of pentagonal dislocation cores separated by strained perfect crystal. This is the same structural unit seen in $SrTiO_3$ and other perovskite-type oxides (Image recorded with the uncorrected 300 kV STEM with 0.13 nm resolution).

Downloaded By: [Oak Ridge National Laboratory] At: 16:07 15 August 2008

Z-contrast imaging [28]. A maximum entropy method [29] was used to decrease the image noise and locate the atomic column positions with an accuracy of around 0.02 nm, as shown in figure 3. The grain boundary was found to consist of a well-ordered array of defect units separated by distorted $SrTiO_3$ unit cells. No second phase or impurity segregation was detected and EELS fine structure indicated octahedral Ti coordination was maintained at the boundary. These defect units are pentagonal in shape with one cation species on the vertices and the two columns of the other cation species contained within the unit. They are geometrically identical to the dislocation cores seen in YBCO (figure 2), with an associated Burgers' vector of 0.39 nm, $\boldsymbol{b} = \boldsymbol{a}[100]$. The cation columns contained within the pentagonal units were found to be spaced closer together than Sr–Sr or Ti–Ti distances found in other compounds. Based on the observation of reduced intensity of these columns and simple valence sum calculations, it was proposed that these columns were not fully occupied.

The schematic of a 28° {410} symmetric tilt boundary in figure 4a makes clear the dislocation content of the structural units, and also shows how the microscopic asymmetry arises as {001} planes terminate alternately from each grain. In figure 4b, the corresponding model for a {310} tilt boundary is shown, containing one less $SrTiO_3$ spacer unit per repeat distance. Thus, the dislocation spacing is not uniform, which raises the elastic energy of the boundary. A transition to dislocation cores on both cation lattices leads to a uniform dislocation spacing along the boundary plane

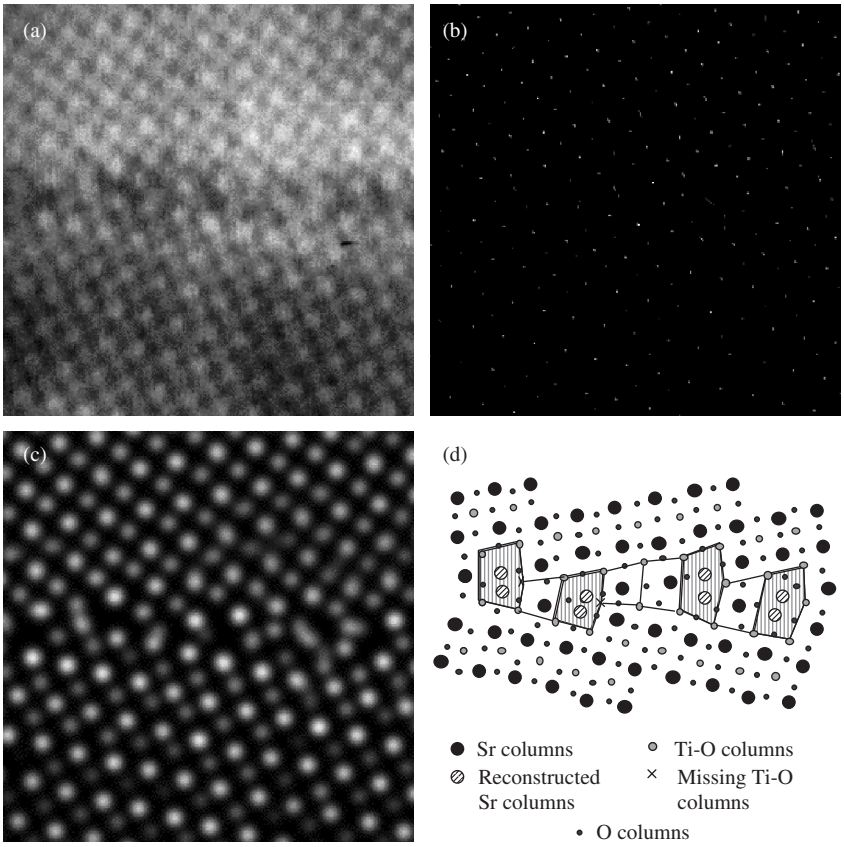

Figure 3. (a) Z-Contrast image of a 24° ⟨001⟩ tilt grain boundary in $SrTiO_3$, with (b) maximum entropy object function, (c) reconstructed image and (d) derived atomic structure with dislocation cores shaded. The boundary is built from an array of the same dislocation cores observed in the low angle boundary, separated by one or two $SrTiO_3$ spacer units (image recorded with the uncorrected 100 kV STEM with 0.22 nm resolution).

Downloaded By: [Oak Ridge National Laboratory] At: 16:07 15 August 2008

and a microscopically symmetric structure. The actual structure is shown in figure 5a, and has relaxed from the proposed symmetric configuration by a small rigid shift.

Many other misorientations, both symmetric and asymmetric, were studied [30, 31], and overall, the structural unit model and the principle of continuity of boundary structure is remarkably successful in predicting most of the structures observed in practice, even though these ideas were proposed based on a much simpler crystal structure [17]. It failed in situations where macroscopic faceting occurred, for example, without faceting, a 45° grain boundary would be comprised of mixtures of {520} and {730} boundary planes giving misorientations of 43.6° and 46.4°, respectively. Instead of adopting these very long and complicated sequences of dislocation cores, the grain boundary plane simply facets onto the {001} and {110} planes, giving short asymmetric segments. Nevertheless, once this fact is known, the structure of the boundary can be constructed with just one additional dislocation

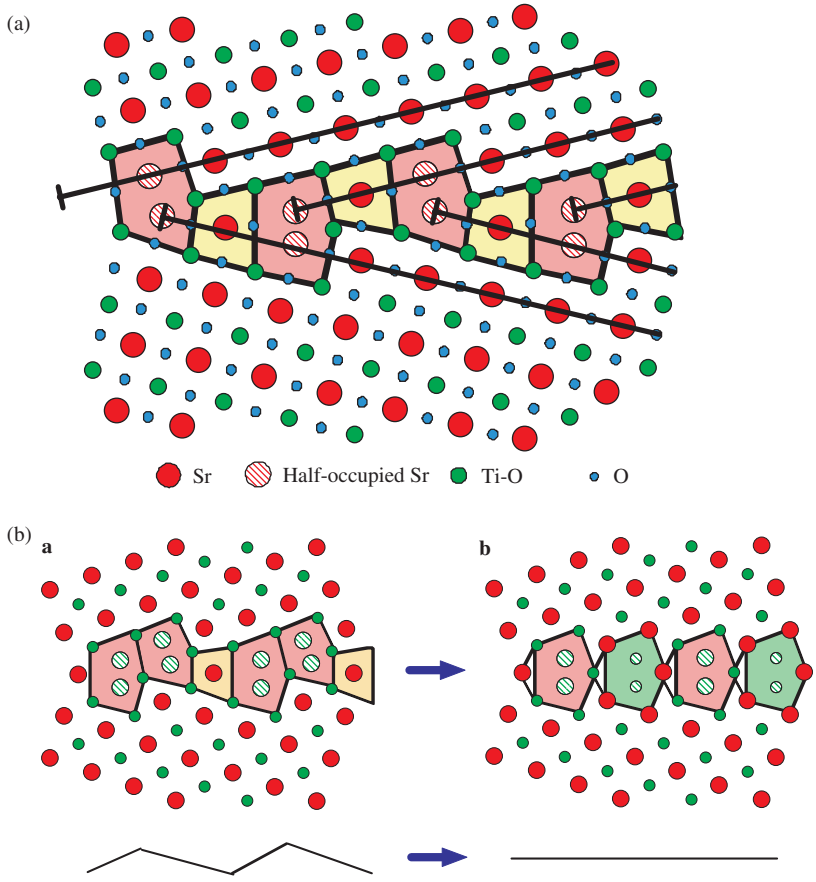

Figure 4. (a) Structure model for the 28° {410} symmetric grain boundary in $SrTiO_3$ showing the dislocation content of the boundary. Note the microscopic asymmetry of the boundary plane despite the fact that the boundary is geometrically symmetric. (b) Transition of a 36° {310} boundary plane from microscopically asymmetric to fully symmetric structure by the incorporation of units on both cation sublattices.

core structure, carrying a Burgers' vector of $\boldsymbol{a}\langle 110\rangle$, as shown in figure 5b. Again, the core can be constructed on either cation sublattice, but only the core with Ti inside Sr columns has so far been observed. The need for two types of dislocations to describe an asymmetric grain boundary is also consistent with the Read–Schockley dislocation model of a grain boundary [16]. It might be expected that the $\boldsymbol{a}\langle 110\rangle$ dislocation core might split into partials when widely spaced. This is indeed the case. Figure 5c shows a 7° symmetric boundary in which the grain boundary plane is close to the {110} plane in both grains. It can be seen that the dislocation has dissociated along the boundary into two partials ($\mathbf{b} = \boldsymbol{a}/2\langle 110\rangle$) separated by a short stacking fault. The core region of both partials appears to have cations located in column positions normally occupied by oxygen in bulk $SrTiO_3$. Further discussions of grain boundary structures can be found in [27, 32, 33].

Downloaded By: [Oak Ridge National Laboratory] At: 16:07 15 August 2008

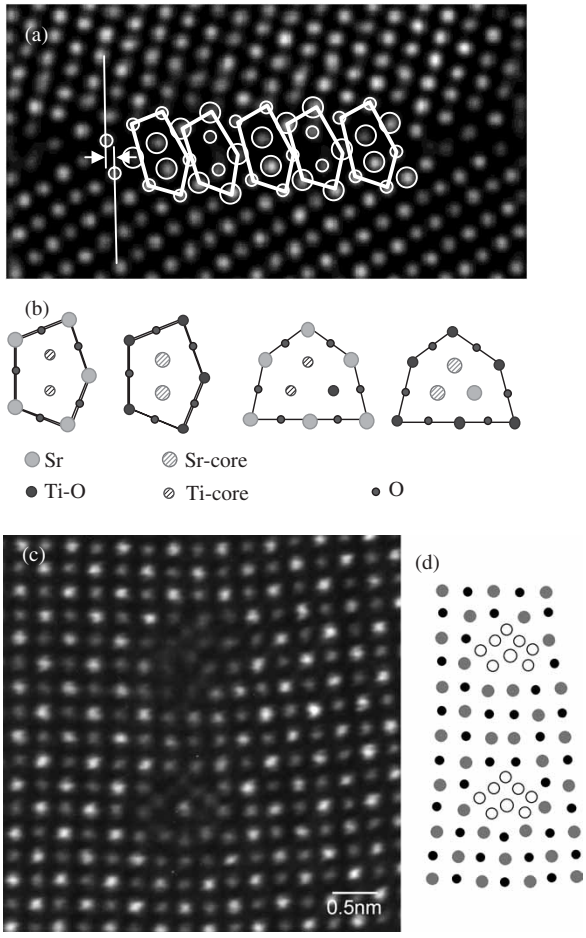

Figure 5. (a) Maximum entropy image of a 36° grain boundary in $SrTiO_3$ showing alternating pentagonal Sr and Ti structural units or dislocation cores. Note the rigid shift compared to the schematic structure of figure 4b. (b) All symmetric and asymmetric ⟨001⟩ tilt boundaries are comprised of specific sequences of these four basic core structures. (c) Z-contrast image of an isolated $\boldsymbol{a}\langle 110\rangle$ dislocation in a low-angle (7°) symmetric $SrTiO_3$ grain boundary in the ⟨001⟩ projection showing dissociation into two partials with $\mathbf{b} = \boldsymbol{a}/2\langle 110\rangle$. (d) Schematic of the dissociated dislocation (open columns are core columns. Images recorded with the uncorrected 300 kV STEM with 0.13 nm resolution).

The macroscopic electrical properties of $SrTiO_3$ are usually explained phenomenologically in terms of double Schottky barriers that are assumed to originate from charged grain boundary planes and the compensating space charge in the adjacent depletion layers [34]. The net result is an electrostatic potential (band bending) that opposes the passage of free carriers through the grain boundary. However, for phenomenological modelling of these effects, a grain boundary charge is usually assumed as an input, and the microscopic origin of this phenomenon has remained elusive. By understanding the nature of the core structure, the origin of the electrical activity can be investigated. If the pair of columns in the dislocation

Downloaded By: [Oak Ridge National Laboratory] At: 16:07 15 August 2008

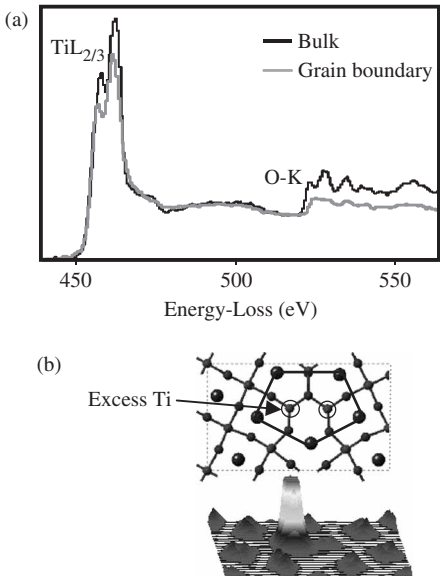

Figure 6. (a) EELS of a low angle grain boundary shows Ti–O ratio is enhanced at the boundary compared to the bulk. (b) Calculation of charge density in the conduction band for a Ti-core structure in which one column has excess Ti and the other is stoichiometric.

Downloaded By: [Oak Ridge National Laboratory] At: 16:07 15 August 2008

core is fully occupied, as in the bulk, the boundary is non-stoichiometric. If, however, they are only half-occupied (e.g. every other site is occupied), the boundary is stoichiometric. This half-occupation has been described as a 'reconstruction' [30, 31]. Occupation cannot be determined simply from the image intensity since columns in the core of a boundary are strained, which can increase or decrease the image intensity depending on the detector angle [9]. The rational for preferring stoichiometric boundaries was that the distance between the pair of columns is usually smaller than in the bulk, which would cause ionic repulsion.

EELS, however, provided definitive evidence of non-stoichiometry [35]. Figure 6a shows the Ti $L_{2,3}$ and O K EELS spectra taken in the bulk and at an individual dislocation core in a low-angle $SrTiO_3$ grain boundary. Normalizing the two spectra to the Ti L-edge continuum it is clear that the Ti–O ratio in the boundary is higher than the bulk. To explore the relative stability of stoichiometric and non-stoichiometric structures, total-energy calculations were carried out. The 53° symmetric {210} ⟨001⟩ tilt grain boundary was used as a model structure, with supercells constructed from either Sr or Ti units. The calculations confirmed that non-stoichiometry was energetically favorable, but found a difference between the two cores. The Sr core preferred half columns of Sr with O vacancies in adjacent columns, i.e. oxygen deficiency. The Ti core preferred full Ti columns, i.e. excess metal compared to the stoichiometric structure.

Electronically, the result is the same. The cations have unbound electrons which must go into the conduction band. Figure 6b shows the spatial distribution of the electrons in the conduction bands for a structure in which one of the two core

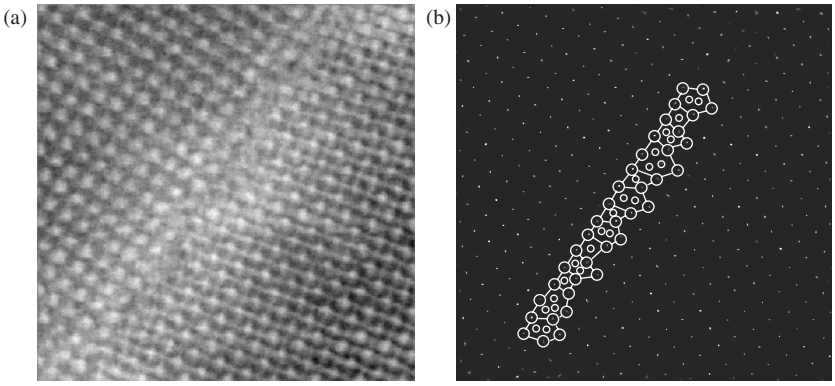

Figure 7. Z-contrast image (a) and maximum entropy atomic column positions (b) of a 30° grain boundary in YBCO, showing the same dislocation cores and sequence as predicted by the structural unit model (Note the ⟨001⟩ axes of the two grains are slightly misoriented degrading the nominal 0.13-nm resolution of the uncorrected 300 kV STEM).

Downloaded By: [Oak Ridge National Laboratory] At: 16:07 15 August 2008

columns is stoichiometric and the other has excess Ti. It is clear that the excess electrons are localized over the excess Ti atoms, maintaining charge neutrality at that site. The calculation of course assumed a pure material, in which there is no band bending and the Fermi level lies near the conduction band. For a boundary surrounded by p-type bulk, these electrons will move off the Ti atoms and annihilate nearby holes. The grain boundary becomes charged and sets up a space-charge region on both sides. Thus, the combination of tools has provided a microscopic explanation for the origin of the grain boundary charge that was postulated from electrical measurements. It arises from the non-stoichiometry of dislocation cores in the perovskite structure.

Similar effects can explain the dramatic effect of grain boundaries in the high temperature superconductors. YBCO is a hole-doped superconductor with about one hole per unit cell for optimum doping. Figure 7 shows an example of a 30° grain boundary in YBCO in which the sequence of units is precisely as expected by direct analogy with $SrTiO_3$ [36]. YBCO also obeys the structural unit model of grain boundaries for both symmetric and asymmetric boundaries.

The superconducting properties of $YBa_2Cu_3O_{7-x}$ are extremely sensitive to oxygen content, changing from superconducting at $x=0$ to insulating at $x=1$. It is not possible to measure such small changes in stoichiometry with sufficient accuracy to determine local superconducting properties, but fortunately, in YBCO the presence of holes in the lower Hubbard band is directly observable by EELS as a pre-edge feature before the main oxygen K-edge. This feature does provide a direct measure of local hole concentration [37, 38]. Figure 8 compares oxygen K-edge spectra obtained from a core, between two cores, and far away from the cores, confirming that there is strong hole depletion in the vicinity of the boundary, strongest at the dislocation cores themselves.

Given the similarity in grain boundary structure to $SrTiO_3$, it was reasonable to assume that YBCO boundaries would also be non-stoichiometric, explaining the observed hole depletion. The variation in the density of structural units with grain

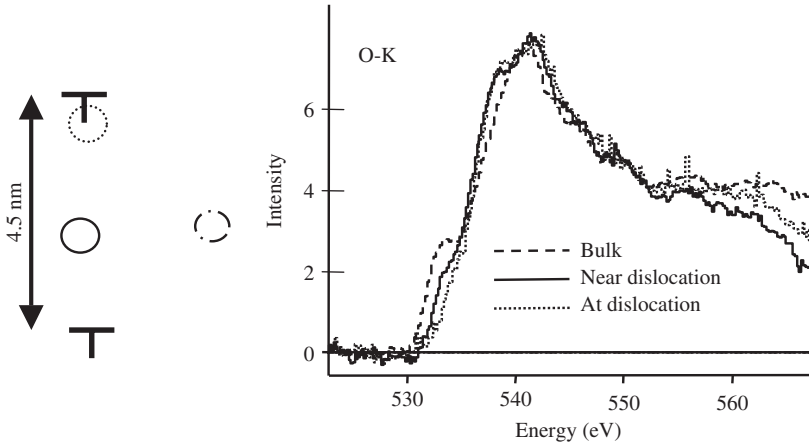

Figure 8. EELS spectra obtained from an 8° grain boundary in YBCO showing strong hole depletion as the probe is moved into a dislocation core.

Downloaded By: [Oak Ridge National Laboratory] At: 16:07 15 August 2008

boundary misorientation is known from the structural unit model. It was well established that the YBCO boundaries were wavy, even when grown on planar bicrystals boundaries, and so asymmetric boundary segments would predominate. Treating the boundary as a pnp layer, the width Δ of the depleted p regions surrounding a boundary is given by $\Delta = \varphi/n$, where φ is the grain boundary charge and n is the bulk charge of one hole per unit cell. Assuming two excess electrons per dislocation core produced a width that increased almost linearly across the entire range of grain boundary misorientations, as shown in figure 9a.

The supercurrent can only pass through this non-superconducting region by some form of tunnelling and must, therefore, show an exponential drop given by $J_c \propto \exp(-2\kappa\Delta)$, where $\kappa = 7.7\,\mathrm{nm}^{-1}$ is a decay constant determined from scanning tunnelling spectroscopy [39, 40]. The predicted decrease in critical current is shown in figure 9b to be an excellent match to the experimental data of [41]. While there are many other possible influences of grain boundaries, including strain [42, 43], and the d-wave nature of the order parameter [44], none can explain the exponential drop across the entire misorientation range. It seems quite remarkable, that with one reasonable assumption, namely a fixed charge per unit length on each dislocation core, the structural unit model so well predicts the dramatic effect of the grain boundary on critical current.

However, it should be noted that this model cannot be expected to fit quantitatively at low grain boundary angles where the dislocation cores become widely separated and the assumption of a planar Josephson junction no longer applies. In this regime, important for coated conductor technologies, misorientation angles are below 4°, and the spacing between dislocations exceeds the superconducting coherence length. A more complicated model is then required to explicitly calculate the pinning potential of a vortex in the strain field of the boundary [45]. It was predicted that perhaps an order of magnitude improvement in critical current might be achieved at a low angle boundary by doping to achieve a flat band condition.

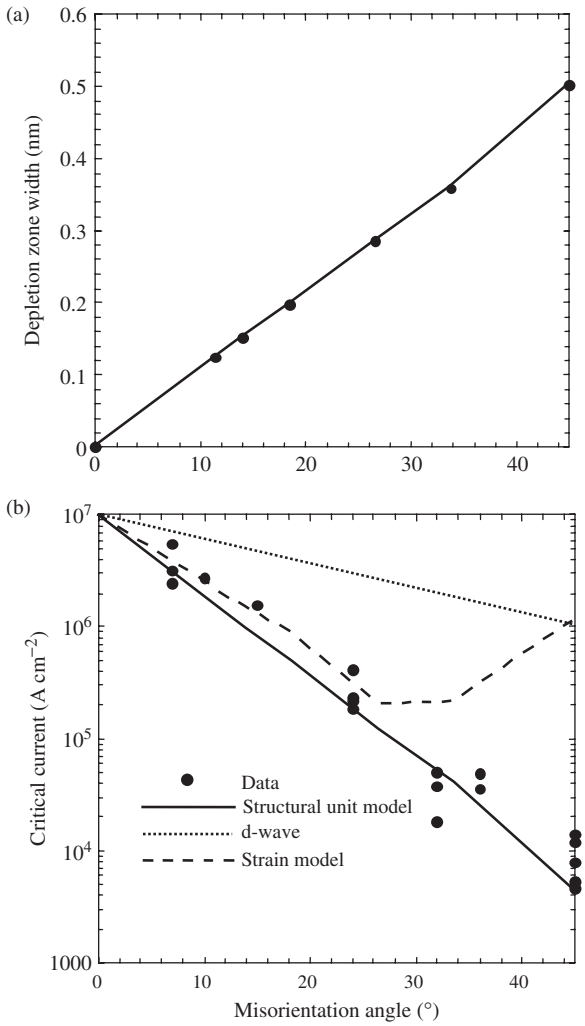

Figure 9. (a) Width of grain boundary depletion zone with misorientation calculated assuming two electrons per structural unit. (b) Exponential drop in grain boundary critical current predicted by the structural unit model compared to the influence of strain and the d-wave nature of the order parameter. Experimental data are from [37].

Downloaded By: [Oak Ridge National Laboratory] At: 16:07 15 August 2008

Various groups have studied the modification of grain boundary properties by chemical doping of the grains. Doping the boundary with Ca was found to increase the critical current, [46, 47], the effect being generally attributed to excess holes introduced by Ca^{2+}-substituting for Y^{3+} as it is known to do in the bulk [48, 49]. Based on the expectation that the boundary plane would be intrinsically non-stoichiometric, first-principles calculations were undertaken to explore the extent of possible effects. The required energy for substituting an isolated Ca dopant atom on different lattice sites in YBCO (in an oxidizing environment) as a function of biaxial strain in the $a-b$ plane is shown in figure 10a. In unstrained YBCO,

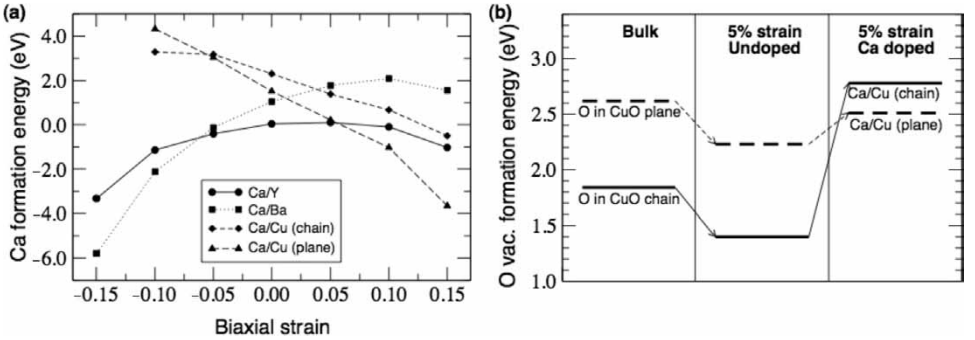

Figure 10. (a) Energy required to substitute Ca on different lattice sites in YBCO as a function of biaxial strain. It is energetically more favourable for Ca to replace Y, Ba or Cu, depending on the local strain. (b) Formation-energy of O vacancies in bulk YBCO (left panel), undoped YBCO under 5% tensile strain in a–b plane (central panel), and Ca-doped YBCO under 5% tensile strain (right panel). For doped grain-boundaries where Ca substitutes Cu, the O vacancy formation-energy increases significantly.

Downloaded By: [Oak Ridge National Laboratory] At: 16:07 15 August 2008

Ca substitutes for Y, as expected. In regions under compression, however, substitution for Ba becomes energetically favourable at strains greater than ~6%. Similarly, in regions under tension, substitution for Cu becomes increasingly favoured. In contrast, strain only has a small effect on substitution for Y. The relative ionic size drives the phenomenon: the ionic radii of Ca and Y are similar, but the radius of Cu is ~30% smaller and the radius of Ba is ~30% larger.

The concomitant strain relief has a major effect on the O vacancy formation energies in the vicinity. Figure 10b shows that in strained, undoped YBCO the formation energies for O vacancies are significantly reduced, both in the CuO_2 planes and CuO chains. O vacancies would, therefore, segregate to an undoped grain-boundary, explaining the oxygen deficiency and hole depletion shown before [36, 38]. However, when Ca doping is introduced, O vacancy formation energies are increased, in the case of the CuO chains, becoming even higher than in the bulk. Hence, the doped grain-boundary should show reduced O deficiency and, therefore, reduced hole depletion. The role of Ca doping is to remove the intrinsic excess of O vacancies from YBCO grain-boundaries. Hence, high critical currents are restored through a cooperative doping mechanism.

Experimental confirmation of this cooperative doping effect was obtained using Z-contrast imaging and EELS. The dislocation core structures were found to be quite different in the Ca-doped case as compared to the undoped sample [50, 51]. As shown in figure 11, the Ca-doped core shows an additional atomic column at its centre, adjacent to the column pair usually observed in this structural unit. The respective core structures were seen consistently along the entirety of each grain boundary. Column-by-column EELS confirmed the scenario predicted by theory, both the expected Ca substitutions and the expected improvement in carrier concentration [51]. Some hole depletion remained, however, indicating some residual weak link behaviour and scope for further improvement in critical current by some more controlled grain boundary doping process, possibly involving a variety of dopants with ionic radii tuned for the different sites in the vicinity of the dislocation core.

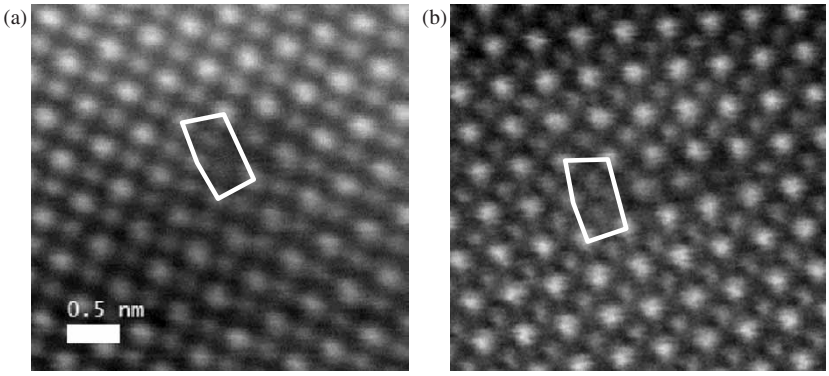

Figure 11. (a) Z-contrast image of pristine 4° [001] tilt grain-boundary dislocation core on the Cu–O sublattice, showing the typical pentagonal arrangement. (b) Ca-doped grain-boundary: the Y/Ba column pentagonal arrangement now encircles three columns, two on the Cu–O and one on the Y/Ba sublattice. The weaker intensity of the Y/Ba column on the left of the core is due to Ca substitution, and the extensive changes in the intensity of the CuO columns to the right of the core are due to substitution of Ba (brighter columns) or Ca (darker columns). EELS verified the compositional changes suggested from the image (Recorded with the aberration-corrected 100 kV STEM with resolution of 0.13 nm).

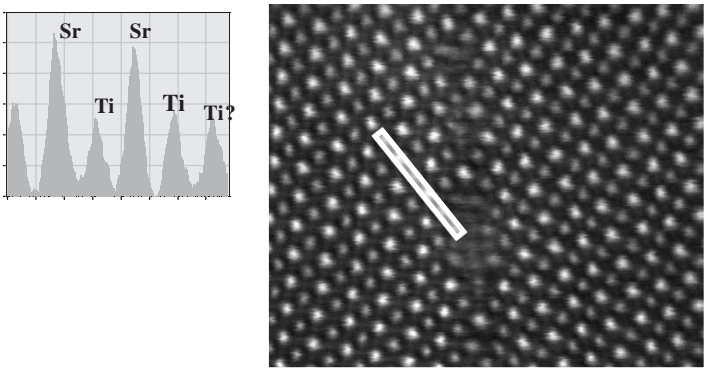

Figure 12. Z-contrast image of a Nb-doped grain boundary in reduced $SrTiO_3$. The intensity trace along the yellow line shows a Sr site at the boundary occupied by Ti, and additional weak columns are visible in the boundary core, suggesting a segregation of Ti oxide (recorded with the aberration-corrected 300 kV STEM with resolution of 0.078 nm).

Grain boundaries in even the prototypical perovskite $SrTiO_3$ can show unexpectedly complex behaviour. Recently, grain boundaries in non-ferroelectric $SrTiO_3$ were found to show ferroelectric behaviour. Using atomic-resolution Z-contrast images and first principles calculations, the origin of the charge was traced to missing oxygen columns in the boundary. The calculated charge density difference showed the presence of dipoles located near the oxygen vacancies [52]. Another example is the effect of annealing in a reducing atmosphere. Figure 12 shows sites in the reduced boundary, in the Sr positions, that show intensities

Downloaded By: [Oak Ridge National Laboratory] At: 16:07 15 August 2008

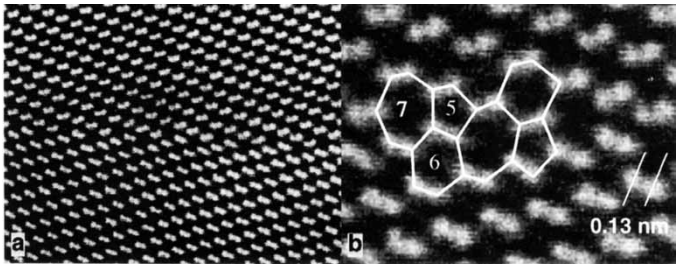

Figure 13. (a) Z-contrast image of a symmetric 39° ⟨110⟩ tilt boundary in silicon as viewed along the ⟨110⟩ tilt axis. (b) Higher magnification view showing the boundary consists of a connected string of Lomer dislocations (the five- and seven-sided structures). The separation between the parallel white lines is 0.13 nm, the silicon column dumbbell separation in this ⟨110⟩ projection (Recorded with the uncorrected 300 kV STEM with 0.13 nm resolution).

Downloaded By: [Oak Ridge National Laboratory] At: 16:07 15 August 2008

expected for TiO columns [53]. In the core of the boundary are several additional columns. Such cores, although supporting a Burgers' vector in the perovskite lattice, can also be considered as filamentary precipitates, perhaps of some Ti oxide, which have formed right along the highly strained region of the dislocation cores. Again, the nature of the dislocation core structure has adapted to local chemical conditions.

3. Semiconductors

A large fraction of high-resolution electron microscopy studies have focused on the relatively open ⟨110⟩ projection of diamond-cubic semiconductors and their defects. The pioneering study of semiconductors at atomic resolution, in fact, examined the atomic structure of a high-angle ⟨110⟩ tilt boundary in germanium [54]. Figure 13 is a Z-contrast image of this same 39° ⟨110⟩ symmetric tilt boundary but in silicon. When looking along the ⟨110⟩ tilt axis, the boundary is seen to contain a continuous stack of projected five- and seven-sided defect structures in place of the six-sided units of the diamond cubic lattice. This defect structure is identical to the core structure of a perfect edge dislocation in silicon with a ⟨110⟩ line direction and an $\boldsymbol{a}/2\langle\bar{1}10\rangle$ Burgers vector. The structure of this Lomer dislocation was first predicted by Hornstra in 1958 [55]. There are no dangling bonds in these defects and bulk-like tetrahedral bonding is maintained in the cores with relatively little distortion to the bond lengths or angles. The image makes it absolutely clear that these dislocation cores can be packed one on top of another and still remain distinct. These edge dislocations are one of only two defect structures found in Si ⟨110⟩ tilt boundaries. The other unit is a twinned version of the six-sided bulk unit. Electronic structure calculations on the $\boldsymbol{a}/2\langle 110\rangle$ edge dislocation in silicon have found the presence of gap states associated with these dislocations despite the absence of dangling bonds [56]. The shifts in the electronic states are correlated with the concentration of strain in the cores; dangling bonds and impurities are not required.

The ⟨001⟩ projection of diamond-cubic materials and their ⟨001⟩ tilt boundaries have been less studied. The principle reason for this is that instruments with resolutions better than 0.15 nm are required to reveal the defect structures in these boundaries. Hornstra [55] again predicted the dislocation structures found in these boundaries long before microscopy had the tools to see them. He proposed that any ⟨001⟩ tilt boundary in diamond-cubic materials would be composed of arrays of two different dislocations. As in the ⟨110⟩ boundaries, only these two structural units have been seen in the ⟨001⟩ tilt boundaries. Figure 14 shows a Z-contrast image of a 23° ⟨001⟩ tilt boundary as viewed along the tilt axis. The boundary is seen to consist of a continuous string of pentagonal and triangular features. This two-dimensional projection was used to calculate the three-dimensional structure of the boundary. From the calculated grain boundary (figure 14), two distinct defect units can be identified. These two units have the same atomic configuration as the two dislocation cores predicted by Hornstra [55]. These defects do not change their structure even though they are spaced every 0.23 nm along the boundary. The units marked 1 and 1′ in the schematic are edge dislocations (⟨001⟩ line direction and $\boldsymbol{a}/2\langle 110\rangle$ Burgers vector) that accommodate the misorientation of the two grains. The units marked 2, 2′, 3 and 3′ are mixed dislocations with equal edge and screw components that are arranged as dipoles. Structurally, the dipoles could be replaced by perfect crystal, so this structure violates the structural unit model. Subsequently, total energy calculations were carried out with and without the dipoles and confirmed that the presence of the dipoles lowers the energy [57]. This effect can be rationalized as follows. The strain field from the grain boundary dislocation array extends into the grains roughly as far as the dislocation separation. Introducing the additional dislocations reduces the extent of the strain field by a factor three. If the cores are not highly distorted, as seen to be the case here, the reduction of far-field strain energy may more than compensate for the additional energy cost of introducing the two new dislocation cores.

Electron microscopy is well suited for the study of the initial stages of misfit dislocation nucleation and of dislocation reactions in strained layer heterostructures.

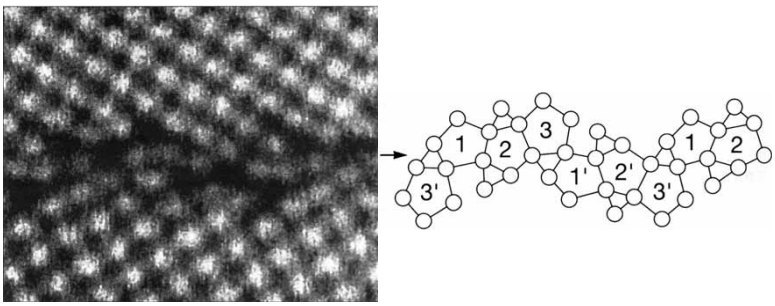

Figure 14. Z-contrast image of a symmetric 23° ⟨001⟩ tilt boundary in silicon and the projected atomic column positions of the boundary core obtained directly from the image. The boundary is found to contain a periodic array (1.38 nm repeat vector) of two distinct defect units. These two defect units have the same atomic configurations as those in perfect edge dislocations (1 and 1′) and mixed dislocations (2, 2′, 3, 3′) seen in bulk silicon (recorded with the uncorrected 300 kV STEM with 0.13 nm resolution).

Downloaded By: [Oak Ridge National Laboratory] At: 16:07 15 August 2008

High-resolution Z-contrast imaging has the added advantage of producing intuitively interpretable images with chemical sensitivity. Thin film formation and misfit accommodation in epitaxial Ge films produced by ion implantation and oxidation of Si (001) wafers has been studied. It has been found that the Ge films, which are constrained to grow layer-by-layer, remain completely coherent with the Si substrate to a thickness of 5–6 nm, as shown in figure 15 [58]. This is 3–6-times thicker that the observed critical thickness for Ge films grown on Si by more conventional deposition techniques. It is observed that misfit accommodating dislocations nucleate at the film surface as Shockley partials. First a 30° partial (so-called because the dislocation Burgers vector is inclined at an angle of 30° to the dislocation line direction) nucleates and glides to the interface, which is followed by a 90° partial which annihilates most of the stacking fault to form a dissociated 60° dislocation located at the Ge/Si interface. With continued oxidation the interface moves into the substrate and the 60°, which glide on inclined {111} planes, sweep the interface. When they encounter another 60° dislocation they will react to form the

Downloaded By: [Oak Ridge National Laboratory] At: 16:07 15 August 2008

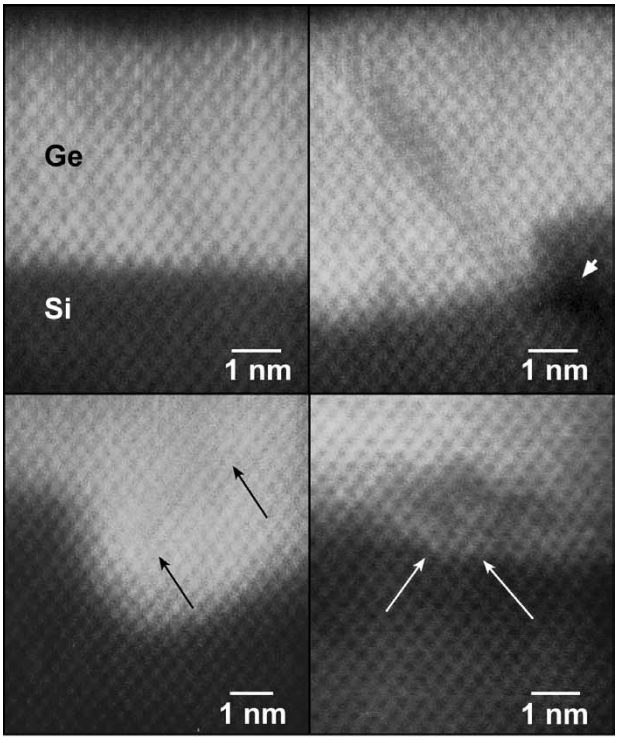

Figure 15. Z-contrast images of epitaxial films of Ge on (001) Si produced by steam oxidation of a silicon wafer implanted with Ge. (1) Dislocation-free 5-nm thick Ge film. (2) Image showing initial stages of misfit accommodation. A 30° Shockley partial dislocation (arrowed) has glided to the Ge/Si interface leaving a stacking fault in the Ge film. (3) Image of a dissociated 60° dislocation with a stacking fault between the two Shockley partial dislocations (arrowed). (4) The energetically preferred perfect edge dislocation (recorded with the uncorrected 100 kV STEM with 0.22 nm resolution).

energetically preferred perfect edge dislocation at the interface. Note how the cores lie entirely in the Ge film.

Z-contrast imaging has also revealed the atomic configurations of misfit dislocations at the heteroepitaxial interfaces of compound semiconductors. In the case of CdTe(001)/GaAs(001), both atomic column positions and type were able to be determined directly from the images [59]. The 60° dislocation cores were found to be located entirely in the CdTe film and to be of the glide set (see, for example, [60] for a discussion of glide versus shuffle set). More surprising was the observation of two different perfect edge dislocation core structures. One set was found to have the structure first proposed by Hornstra [55] for diamond cubic materials. These cores were seen to straddle the interface. The other set, orthogonal to the first, was seen to have an asymmetric core structure that differs from the Hornstra model. These cores sit above the interface, in the CdTe film and contain Cd columns that appear to have only three bonds. Although the concept of asymmetric core structures has been proposed for both Si and compound semiconductors, no direct evidence for their existence had been published. Novel core structures have also been seen at GaAs/Si interfaces [61]. More detailed analysis of the physical and electrical properties of these defects is now possible using such images as a foundation from which to proceed. An excellent example of such studies in the GaN system is given in the article by Arslan *et al.* [62] in this issue.

Downloaded By: [Oak Ridge National Laboratory] At: 16:07 15 August 2008

4. Direct observation of impurity segregation at dislocation cores

Segregation of impurities to the same 23° Si ⟨001⟩ tilt boundary discussed above was directly observed by Z-contrast imaging. An arsenic-doped boundary clearly showed columns 20% brighter on average than other similar columns, indicating the presence of segregated As atoms (figure 16) [63]. The increased intensity corresponds to an average of only 5% As concentration, approximately two As atoms in each atomic column. Density functional calculations added significant further insight, indicating that isolated As atoms have a small segregation energy of ~0.1 eV at all the boundary sites. With no clear preference for any site, the observed extra intensity was not due to isolated segregant atoms. However, calculations for arsenic 'chains' in various columns of the boundary revealed higher segregation energies (0.25–0.30 eV/As atom) at the same triangular features where extra intensity is

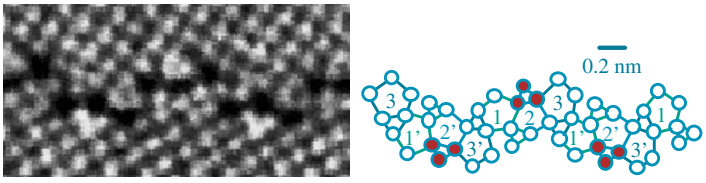

Figure 16. Z-contrast image of the As-doped 23° [001] tilt grain boundary in Si. Columns shown shaded in the schematic are those seen brighter in the image due to segregated As (recorded with the uncorrected 300 kV STEM with 0.13 nm resolution).

observed in the figure. At all other sites in the boundary the segregation energies remained ~0.1 eV/As atom. Arsenic segregates only to one of the three distinct dislocation cores that form the boundary, the mixed dislocation at the centre of each sequence, labelled 2 or 2′. This atomic-scale picture of segregation highlights how precise atomic configurations of host atoms and impurities determine important segregation phenomena.

Z-contrast imaging of an MgO grain boundary (figure 17) [64] revealed a structure that was inconsistent with the widely accepted structure of that boundary proposed by Harris *et al.* [65] based on theoretical modelling using classical potentials. The observed structure was similar to one proposed much earlier by Kingery [66]. These two structures are compared in figure 17, where the large empty core of the Harris structure is obviously very different from the more dense core of the Kingery model. However, it is apparent in the experimental image that certain specific atomic columns at the grain boundary are significantly brighter than neighbouring columns, as arrowed in the figure, suggesting that impurities, with $Z > 12$, may be segregated at these sites despite the fact that the boundary was not intentionally doped. EELS measurements indeed established that significant concentrations of Ca are present in the grain boundary, 0.3 monolayers, consistent with the bright intensity in the image.

To reconcile these observations with the prior experimental and theoretical work, first-principles theoretical calculations were performed. These calculations, in fact, reproduced the results of the classical potential calculations for the clean grain boundary, indicating the open structure to be 0.5 eV lower in energy per periodic repeat unit. Theory further determined that Ca has a large segregation energy in both boundary structures, but significantly higher in the dense structure, sufficient to make the dense structure the lower energy boundary. These calculations, therefore,

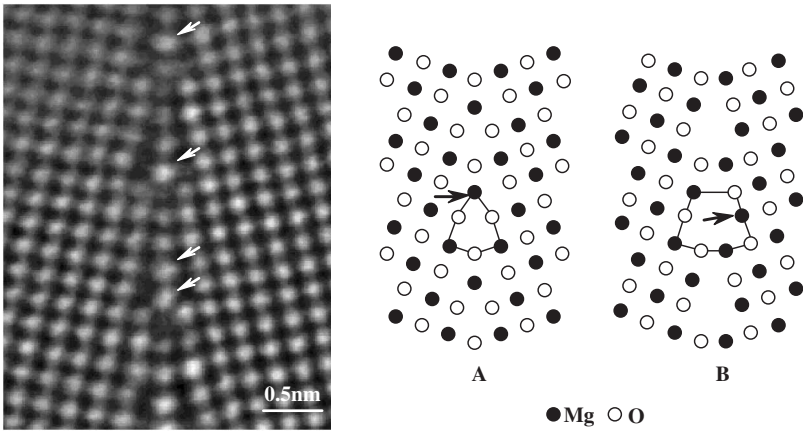

Figure 17. Z-contrast image from a 24° ⟨001⟩ tilt grain boundary in MgO showing occasional bright atomic columns at the grain boundary (arrowed), compared to two structures for the 36° ⟨001⟩ tilt grain boundary proposed by (A) Kingery [66] and (B) Harris *et al.* [65]. Sites of Ca segregation are arrowed (Recorded with the uncorrected 300 kV STEM with 0.13 nm resolution).

Downloaded By: [Oak Ridge National Laboratory] At: 16:07 15 August 2008

establish that the dense structure is in fact stabilized by the Ca segregation, a segregation-induced structural transformation. Examination of the electronic charge distribution revealed just a small perturbation to the oxygen ions next to the Ca atom, indicating the transformation is structural not electronic in origin, i.e. it is driven by the size difference between Ca and Mg.

A long-standing issue solved by the application of Z-contrast STEM and first-principles theory is the embrittlement of Cu by Bi, a classic example of the phenomenon. The link between Bi segregation and grain boundary faceting was well known [67], but no atomistic explanation of the embrittlement had been established. Figure 18 compares Z-contrast images of non-doped (a) and Bi-doped (b) boundaries in Cu [68]. In this [001] projection, the atomic columns in the Cu grains form a square grid of bright dots separated by 0.18 nm. The boundary in both samples is seen to consist of a periodic array of triangular and pentagonal structural units carrying Burger's vectors of $\boldsymbol{a}\langle 100\rangle$. One of the four under-coordinated atomic columns in each structural unit of the Bi-doped boundary is seen to be distinctly bright, consistent with the presence of Bi. The images make it clear that this grain boundary configuration is little affected by the presence of Bi, which simply substitutes for Cu on a preferred atomic site in the boundary.

The electronic structure of the grain boundary region can be measured directly with EELS. It is found that locally the Cu-L_3 edge is affected by the presence of Bi in the boundary [68]. The changes are consistent with a reduction of the density of d-like states at the Fermi level and reduced hybridization between d and s states for the Cu atoms that surround the Bi. Both of these results also imply reduced covalent (directional) bonding among Cu3d electrons in the boundary region.

Density functional calculations of the Cu-L_3 edge in the Bi-doped grain boundary show a reduction of all three maxima present in the near edge structure, compared to the calculated Cu bulk near edge structure, just as was seen experimentally. The calculations confirm the interpretation of the experimental EELS results that there are a reduced number of unoccupied d states at or above the Fermi level and reduced hybridization between d and s states for the Cu atoms that surround the Bi impurities. The calculated charge density difference also revealed that Bi induces a slight reduction in the directionality of bonding between Cu atoms. In addition, the calculations show enhanced electron density at the Cu sites that surround the Bi impurity. This means that electrons further fill the usually half-filled s-bands of Cu, reducing the bond strength between the Cu atoms that surround the Bi impurity, explaining the embrittlement.

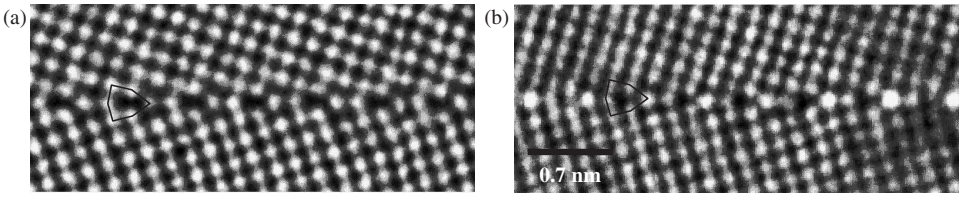

Figure 18. Z-contrast images of the grain boundary region of a symmetric 36.8° ⟨001⟩ tilt boundary in (a) pure Cu and (b) Bi-doped Cu. The Bi segregation sites in (b) are seen to be distinctly bright (recorded with the uncorrected 300 kV STEM with 0.13 nm resolution).

Downloaded By: [Oak Ridge National Laboratory] At: 16:07 15 August 2008

5. Complex dislocation core structures

Intermetallics are expected to be the key to building high-performance jet engines and other high-temperature, high-performance structures. However, the poor low-temperature ductility of these compounds has hindered their commercial development for decades. The improved resolution of the aberration-corrected microscope is able to provide new insight into the atomic structure of dislocation cores in complex materials. Z-contrast imaging revealed that the synchroshear dislocation core in the C14 variant of Cr_2Hf contained 'extra' Cr columns, as shown in figure 19 [69]. During dislocation motion the Cr atoms must move into and out of these columns. Diffusion is, therefore, necessary, which hinders their motion and contributes to the brittleness of this material at low temperatures. From geometric considerations dislocation motion would be expected to involve only glide, but, by revealing the non-stoichiometric nature of the core, the reason for the slow dislocation motion is clear. Realistic theoretical modelling of the slip process could now be undertaken to unravel the key atomic configurations that define the energy barrier leading to a true atomistic understanding of the factors determining the energy barrier, and helping pave the way for the design of new alloys with optimized mechanical properties.

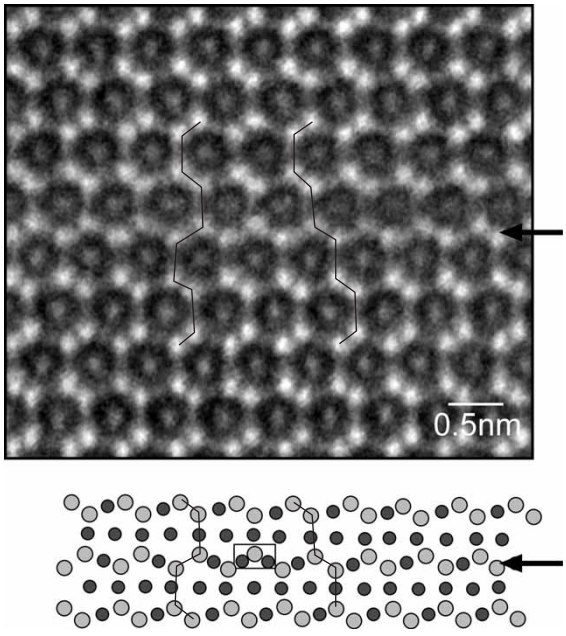

Figure 19. Z-contrast image of a synchroshear dislocation core in Cr_2Hf intermetallic. A stacking fault comes in from the right (arrowed). As shown in the schematic, the core contains additional Cr columns so that dislocation glide cannot occur just by slip processes, but must involve atomic diffusion, accounting for the poor low-temperature ductility of this material (recorded with the aberration-corrected 300 kV STEM with 0.078 nm resolution).

Downloaded By: [Oak Ridge National Laboratory] At: 16:07 15 August 2008

Another example of a complex dislocation core structure is shown in the structural ceramic α-Al_2O_3. The nature of the terminating column has been controversial [70, 71]. In this case, because of the low signal on the Z-contrast image from the light material, the bright-field phase-contrast image showed better contrast. An unanticipated benefit of aberration correction in the STEM has been that it becomes possible to collect an efficient, aberration-corrected, bright-field phase-contrast image. The reason is that aberration correction removes the rapid oscillations of the phase-contrast transfer function, which not only extends the resolution, the original motivation for aberration correction, but also substantially relaxes the coherence requirements. As a result, good phase-contrast imaging can be achieved with beam divergence 10 times greater than before, translating into 100 times the collection efficiency for bright-field STEM. In this case, the images clearly show that the dislocation slip plane is located in between the Al and O layers and unambiguously reveal that the individual dislocation cores are surprisingly non-stoichiometric in this ionic compound. Again, from such knowledge, density functional calculations of the barrier to glide will become feasible.

Downloaded By: [Oak Ridge National Laboratory] At: 16:07 15 August 2008

6. Future directions

It is clear from the examples presented that dislocation cores are identifiable topological defects not only when isolated but also when arranged into arrays to form grain boundaries. The structural unit model works only in certain cases, however. It works remarkably well in undoped YBCO, a very complex structure, but one in which the dislocation core structure changes in response to chemical potential. It does not work in the elemental semiconductor Si, where cores are less adaptable; tetrahedral bonding was maintained and dislocation dipoles inserted to reduce the long-range elastic stresses. Impurity segregation can also introduce dislocation core transformations and the atomic size is the driving force in the oxides. In contrast, the driving force for Bi embrittlement in Cu appears to be electronic in origin. These examples demonstrate that although much has been learnt about core structures, much still remains poorly understood.

It is clear that we have the required tools, the aberration-corrected STEM combined with first-principles calculations. The benefits of aberration correction appear obvious; better resolution resolves finer details of dislocation core structures. However, the benefits extend much further than a 'mere' factor of two increase in resolution might suggest. The smaller probe also brings improved image contrast and improved signal to noise ratio. When the probe is located over one atomic column, a much higher fraction of the incident current goes down that particular column instead of intersecting adjacent columns. The benefit also applies to EELS, and the spectroscopic identification of an individual atom within a crystal has recently been demonstrated [72].

Aberration corrected STEM has also brought some unanticipated benefits. First, is the ability to form a simultaneous, aberration-corrected phase-contrast image, as shown in figure 20. Although not as efficient as the parallel imaging of conventional TEM, the fact that it is available from the same area of specimen as

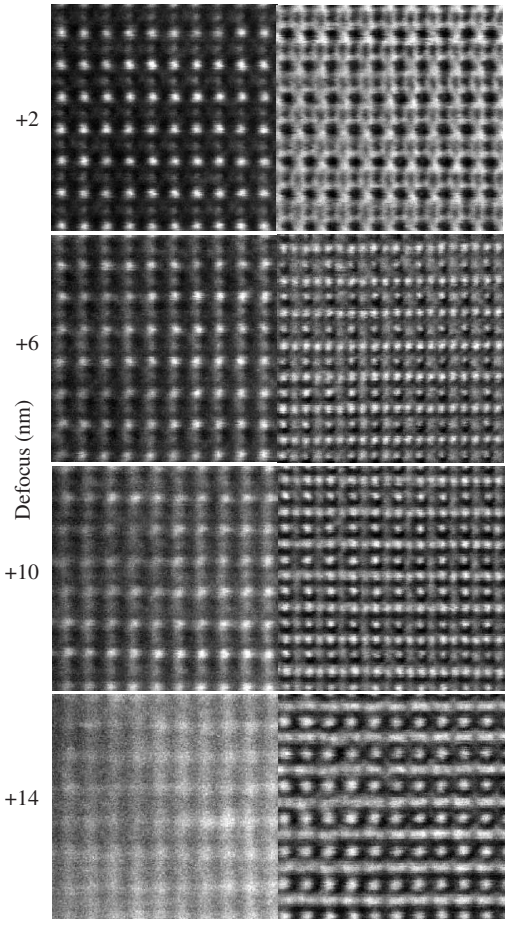

Figure 20. Through focal series of simultaneously acquired Z-contrast (left) and bright-field phase-contrast (right) images of $SrTiO_3$ in the ⟨110⟩ projection. Both images are aberration corrected. The incoherent Z-contrast image has optimum defocus at 2 nm, with the Sr columns brightest, the Ti less bright and the O columns barely visible in between the Ti columns. The image becomes progressively out of focus as the defocus is increased. The phase-contrast image shows the O columns clearly at a defocus of 6 nm (recorded with the aberration-corrected 300 kV STEM with resolution of 0.078 nm in Z-contrast).

examined with EELS and Z-contrast imaging, without any change in operating conditions, means that the advantages of both kinds of images are readily available. Secondly, aberration correction achieves the higher resolution by increasing the angular range contributing to the probe. As a result the depth of focus is reduced, and a through-focal series becomes a through-depth series. It becomes possible to perform a 3D reconstruction in a similar manner as used for confocal optical microscopy [73]. A spectacular example is the imaging of individual Hf atoms within a sub-nanometer SiO_2 layer sandwiched between a Si substrate and a HfO_2 high dielectric constant layer, a test structure for future generation devices [74].

Downloaded By: [Oak Ridge National Laboratory] At: 16:07 15 August 2008

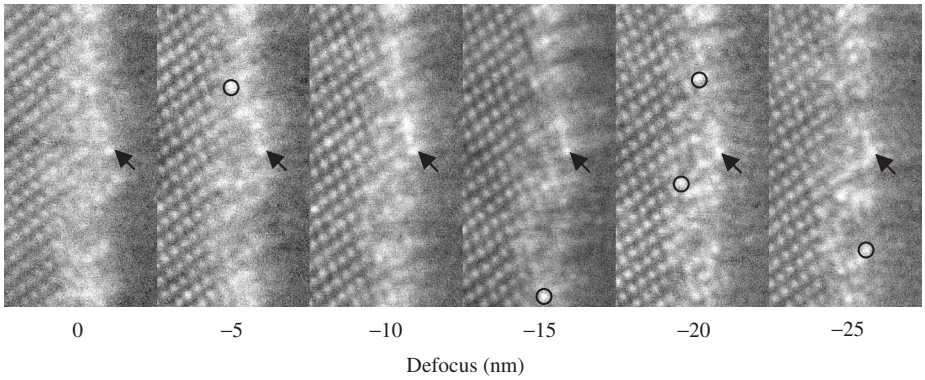

Figure 21. Through focal series of Z-contrast images from a La-doped Al_2O_3 grain boundary that does not have a simple planar interface. Some La atoms show maximum contrast at one depth (circled) consistent with the focus behaviour of an isolated dopant atom, while others show consistently in all frames, indicative of a columnar occupation (recorded with the aberration-corrected 300 kV STEM with resolution of 0.078 nm; courtesy N. Shibata, Y. Ikuhara and A. Y. Borisevich).

Downloaded By: [Oak Ridge National Laboratory] At: 16:07 15 August 2008

Present aberration correctors correct for the third-order geometric aberrations, but plans are underway for correctors able to compensate up to fifth-order aberrations. These will provide depth resolution ~1 nm, and it will become feasible to extend our studies on dislocations and grain boundaries beyond those that have a simple projection. A depth sequence from a high-angle La-doped grain boundary that does not have a sharp planar interface is shown in figure 21. Some features show similar contrast in all frames, indicative of several impurity atoms segregated at different depths with the same lateral position. This could be partial occupation of an atomic column or repeated occupation of a grain boundary facet site, for example. Other features show strong contrast in one specific frame, with no La atoms directly above or below. It is difficult to interpret such data at the present time because, in a crystal, channelling tends to work against focusing the beam at a unique depth. Channelling effects become progressively less important as the probe convergence angle is enlarged [75], and in future generations of aberration-corrected STEMs it should be feasible to find strategies to overcome these problems, such as combined on- and off-axis imaging to maximize both lateral and depth resolution. It will be feasible to investigate dislocation core structures in higher order grain boundaries or buried grain boundaries inside a polycrystalline matrix, the only remaining situation where the dislocation model of grain boundaries remains to be verified.

We can also look forward to combining the single atom EELS sensitivity with depth resolution, probing the electronic environment of a single impurity atom located on a dislocation core, finally revealing their precise atomic sites and local electronic structure. Together with theory, many remaining issues will certainly become clarified, for example, how Cottrell atmospheres control dislocation motion, how impurities or non-stoichiometry determine electrical activity along threading

dislocations or grain boundaries, and the actual atomic positions and interatomic forces during slip and fracture processes.

Acknowledgements

The authors are grateful to many colleagues for the collaborations mentioned in this article, including S. T. Pantelides, N. D. Browning, G. Duscher, T. Kaplan, M. Kim, D. K. Christen, R. F. Klie, Y. Zhu, J. Buban, A. Franceschetti, P. Pradhumarashi, V. P. Dravid, A. Maiti, Y. Yan, S. Kumar, P. Hazzledine, N. Shibata, Y. Ikuhara, W. H. Sides Jr., K. van Benthem, A. Y. Borisevich, A. R. Lupini, A. J. McGibbon, M. M. McGibbon, M. Varela and J. T. Luck. This research was sponsored by the Division of Materials Sciences and Engineering, Office of Basic Energy Sciences, US Department of Energy, under contract DE-AC05-00OR22725 with Oak Ridge National Laboratory, managed and operated by UT-Battelle, LLC.

Downloaded By: [Oak Ridge National Laboratory] At: 16:07 15 August 2008

References

[1] C.V. Burton, Phil. Mag. **33** 191 (1892).
[2] G.I. Taylor, Proc. R. Soc. Lond. Ser. A **145** 388 (1934).
[3] J.M. Burgers, Proc. Kon. Ned. Akad. Wet. **42** 293 (1939).
[4] F.C. Frank and J.H. van der Merwe, Proc. R. Soc. Lond. Ser. A **198** 216 (1949).
[5] W. Bollmann, Phys. Rev. **103** 1588 (1956).
[6] P.B. Hirsch, R.W. Horne and M.J. Whelan, Phil Mag. **1** 677 (1956).
[7] J.W. Menter, Proc. R. Soc. Lond. Ser. A **236** 119 (1956).
[8] S.J. Pennycook and P.D. Nellist, in *Impact of Electron and Scanning Probe Microscopy on Materials Research*, edited by D.G. Rickerby, U. Valdré and G. Valdré (Kluwer, Dordrecht, 1999), p. 161.
[9] P.D. Nellist and S.J. Pennycook, in *Advances in Imaging and Electron Physics*, edited by B. Kazan, T. Mulvey and P. Hawkes, Vol. 113 (Elsevier, New York, 2000), p. 147.
[10] D.E. Jesson and S.J. Pennycook, Proc. R. Soc. Lond. A **441** 261 (1993).
[11] D.E. Jesson and S.J. Pennycook, Proc. R. Soc. Lond. A **449** 273 (1995).
[12] G. Duscher, N.D. Browning and S.J. Pennycook, Phys. Status Solidi A **166** 327 (1998).
[13] N.D. Browning, M.F. Chisholm and S.J. Pennycook, Nature **366** 143 (1993).
[14] X. Xu, S.P. Beckman, P. Specht, *et al.*, Phys. Rev. Lett. **95** 145501 (2005).
[15] Y. Xin, S.J. Pennycook, N.D. Browning, *et al.*, Appl. Phys. Lett. **72** 2680 (1998).
[16] W.T. Read and W. Shockley, Phys. Rev. B **78** 275 (1950).
[17] A.P. Sutton and V. Vitek, Phil. Trans. R. Soc. Lond. A. **309** 1 (1983).
[18] J.G. Bednorz and K.A. Muller, Z. Phys. B **64** 189 (1986).
[19] J.W. Elkin, A.I. Braginski, A.J. Panson, *et al.*, J. Appl. Phys. **62** 4821 (1987).
[20] J. Mannhart, P. Chaudhari, D. Dimos, *et al.*, Phys. Rev. Lett. **61** 2476 (1988).
[21] D. Dimos, P. Chaudhari, J. Mannhart, *et al.*, Phys. Rev. Lett. **61** 219 (1988).
[22] D. Dimos, P. Chaudhari and J. Mannhart, Phys. Rev. B **41** 4038 (1990).
[23] Z.G. Ivanov, P.A. Nilsson, D. Winkler, *et al.*, Appl. Phys. Lett. **59** 3030 (1991).
[24] R. Gross and B. Mayer, Physica C **180** 235 (1991).
[25] M.F. Chisholm and D.A. Smith, Phil. Mag. A **59** 181 (1989).

[26] M.F. Chisholm and S.J. Pennycook, Nature **351** 47 (1991).
[27] S.J. Pennycook, C. Prouteau, M.F. Chisholm, *et al.*, in *Studies in High-Temperature Superconductors: Microstructural Studies in HTSC*, edited by A.V. Narlikar, Vol. 30 (Nova Science, New York, 2000).
[28] M.M. McGibbon, N.D. Browning, M.F. Chisholm, *et al.*, Science **266** 102 (1994).
[29] A.J. McGibbon, S.J. Pennycook and D.E. Jesson, J. Microsc. **195** 44 (1999).
[30] M.M. McGibbon, N.D. Browning, A.J. McGibbon, *et al.*, Phil. Mag. A **73** 625 (1996).
[31] N.D. Browning, S.J. Pennycook, M.F. Chisholm, *et al.*, Interface Sci. **2** 397 (1995).
[32] N.D. Browning, J.P. Buban, C. Prouteau, *et al.*, Micron **30** 425 (1999).
[33] N.D. Browning, M.F. Chisholm and S.J. Pennycook, in *Characterization of High-Tc Materials and Devices by Electron Microscopy*, edited by N.D. Browning and S.J. Pennycook (Cambridge University Press, Cambridge, 2000).
[34] M. Vollman and R. Waser, J. Am. Ceram. Soc. **77** 235 (1994).
[35] M. Kim, G. Duscher, N.D. Browning, *et al.*, Phys. Rev. Lett. **86** 4056 (2001).
[36] N.D. Browning, J.P. Buban, P.D. Nellist, *et al.*, Physica C **294** 183 (1998).
[37] N.D. Browning, M.F. Chisholm, S.J. Pennycook, *et al.*, Physica C **212** 185 (1993).
[38] N.D. Browning, J. Yuan and L.M. Brown, Physica C **202** 12 (1992).
[39] J. Halbritter, Phys. Rev. B **48** 9735 (1993).
[40] J. Halbritter, Phys. Rev. B **46** 14861 (1992).
[41] H. Hilgenkamp and J. Mannhart, Appl. Phys. Lett. **73** 265 (1998).
[42] A. Gurevich and E.A. Pashitskii, Phys. Rev. B **57** 13878 (1998).
[43] M.F. Chisholm and S.J. Pennycook, Nature **351** 47 (1991).
[44] H. Hilgenkamp, J. Mannhart and B. Mayer, Phys. Rev. B **53** 14586 (1996).
[45] D. Agassi, D.K. Christen and S.J. Pennycook, Appl. Phys. Lett. **81** 2803 (2002).
[46] G. Hammerl, A. Schmehl, R.R. Schulz, *et al.*, Nature **407** 162 (2000).
[47] A. Schmehl, B. Goetz, R.R. Schulz, *et al.*, Europhys. Lett. **47** 110 (1999).
[48] J.T. Kucera and J.C. Bravman, Phys. Rev. B **51** 8582 (1995).
[49] H.B. Su and D.O. Welch, Supercond. Sci. Technol. **18** 24 (2005).
[50] X. Song, G.D. Daniels, M. Feldmann, *et al.*, Nature Mater. **4** 470 (2005).
[51] R.F. Klie, J.P. Buban, M. Varela, *et al.*, Nature **435** 475 (2005).
[52] R. Shao, M.F. Chisholm, G. Duscher, *et al.*, Phys. Rev. Lett. **95** 197601 (2006).
[53] P. Prabhumirashi, V.P. Dravid, A.R. Lupini, *et al.*, Appl. Phys. Lett. **87** 121917 (2005).
[54] O.L. Krivanek, S. Isoda and K. Kobayashi, Phil. Mag. **36** 931 (1977).
[55] J. Hornstra, J. Phys. Chem. Solids **5** 129 (1958).
[56] F. Liu, M. Mostoller, V. Milman, *et al.*, Phys. Rev. B **51** 17192 (1995).
[57] J.R. Morris, Z.Y. Lu, D.M. Ring, *et al.*, Phys. Rev. B **58** 11241 (1998).
[58] M.F. Chisholm, S.J. Pennycook and D. Jesson, in *Atomic Scale Structure of Interfaces*, edited by R.D. Bringens, R.M. Feenstra and J.M. Gibson, Vol. 159 (Materials Research Society, Warrendale, PA, 1990), p. 447.
[59] A.J. McGibbon, S.J. Pennycook and J. Angelo, Science **269** 519 (1995).
[60] J.P. Hirth and J. Lothe, *Theory of Dislocations* (Wiley, New York, 1982), pp. 378–382.
[61] S. Lopatin, S.J. Pennycook, J. Narayan, *et al.*, Appl. Phys. Lett. **81** 2728 (2002).
[62] I. Arslan, A. Bleloch, E. Stach, *et al.*, Phil. Mag. (2006), this issue
[63] M.F. Chisholm, A. Maiti, S.J. Pennycook, *et al.*, Phys. Rev. Lett. **81** 132 (1998).
[64] Y. Yan, M.F. Chisholm, G. Duscher, *et al.*, Phys. Rev. Lett. **81** 3675 (1998).
[65] D.J. Harris, G.W. Watson and S.C. Parker, Phil. Mag. A **74** 407 (1996).
[66] W.D. Kingery, J. Am. Ceram. Soc. **57** 1 (1974).
[67] W. Sigle, L.S. Chang and W. Gust, Phil. Mag. A **82** 1595 (2002).
[68] G. Duscher, M.F. Chisholm, U. Alber, *et al.*, Nature Mater. **3** 621 (2004).
[69] M.F. Chisholm, S. Kumar and P. Hazzledine, Science **307** 701 (2005).
[70] J.B. BildeSorensen, B.F. Lawlor, T. Geipel, *et al.*, Acta Mater. **44** 2145 (1996).

Downloaded By: [Oak Ridge National Laboratory] At: 16:07 15 August 2008

[71] M.L. Kronberg, Acta Mater. **5** 507 (1957).
[72] M. Varela, S.D. Findlay, A.R. Lupini, *et al.*, Phys. Rev. Lett. **92** 095502 (2004).
[73] A.Y. Borisevich, A.R. Lupini and S.J. Pennycook, Proc. Natl. Acad. Sci. USA **103** 3044 (2006).
[74] K. van Benthem, A.R. Lupini, M. Kim, *et al.*, Appl. Phys. Lett. **87** 034104 (2005).
[75] A.Y. Borisevich, A.R. Lupini, S. Travaligni, *et al.*, J. Elect. Microsc. **55** 7 (2006).

Downloaded By: [Oak Ridge National Laboratory] At: 16:07 15 August 2008